



# DROP-IT

## DELIVERABLE 1.3

### Homogeneous thin films of B-LFP nanocrystals and properties

**Due date of deliverable: 2020/10/31**

**Actual submission date: 2020/12/21**

DELIVERABLE number: D1.3  
Due date: 31.10.2020  
Nature<sup>1</sup>: R  
Dissemination Level<sup>1</sup>: PU  
Work Package: WP1  
Lead Beneficiary: PARTNER 1 - UVEG  
Contributing Beneficiaries: UVEG, UJI, ETHZ, AVA, SRI, INSA

---

<sup>1</sup> **Nature:** R = Report, P = Prototype, D = Demonstrator, O = Other

**Dissemination level** PU = Public PP = Restricted to other programme participants (including the Commission Services) RE = Restricted to a group specified by the consortium (including the Commission Services) CO = Confidential, only for members of the consortium (including the Commission Services) Restraint UE = Classified with the classification level "Restraint UE" according to Commission Decision 2001/844 and amendments Confidential UE = Classified with the mention of the classification level "Confidential UE" according to Commission Decision 2001/844 and amendments Secret UE = Classified with the mention of the classification level "Secret UE" according to Commission Decision 2001/844 and amendments



This project has received funding from the European Union's Horizon 2020 research and innovation programme under **Grant Agreement No. 862656**.



DOCUMENT HISTORY

<b>Version</b>	<b>Date</b>	<b>Reason of change</b>
1	2020/04/24	Contribution from UVEG
2	2020/04/26	Contribution from UJI
3	2020/04/28	Contribution from ETHZ
4	2020/04/29	Contribution from Avantama
5	2020/04/29	Contribution from INSA Rennes
6	2020/04/30	Edition by UJI and UVEG
7	2020/11/20	Update with results of new materials - UVEG and SRI
8	2020/12/02	Revision by UVEG
9	2020/12/16	Further contribution and revision by UVEG





## Contents

<b>1 DELIVERABLE DESCRIPTION .....</b>	<b>4</b>
<b>2 RESULTS ON DIFFERENT PEROVSKITE MATERIALS .....</b>	<b>5</b>
<b>2.1 PREPARATION OF FILMS .....</b>	<b>6</b>
<b>2.2 OPTICAL PROPERTIES OF THIN FILMS OF POSSIBLE B-LFP NANOCRYSTALS.....</b>	<b>8</b>
<b>2.2.1 FILMS OF TIN (SN)-BASED PEROVSKITE NANOCRYSTALS: FASNI<sub>3</sub> .....</b>	<b>8</b>
<b>2.2.2 FILMS OF TIN (SN)-BASED PEROVSKITE NANOCRYSTALS: CS<sub>2</sub>SNI<sub>6</sub>.....</b>	<b>18</b>
<b>2.2.3 FILMS OF CS<sub>3</sub>BI<sub>2</sub>I<sub>9</sub> NANOCRYSTALS .....</b>	<b>15</b>
<b>2.2.4 FILMS OF NANOCRYSTALS OF RUDORFFITES AG<sub>2</sub>BI<sub>5</sub> AND AG<sub>3</sub>BI<sub>6</sub> .....</b>	<b>19</b>
<b>2.3 OPTICAL PROPERTIES OF MICROCRYSTALLINE POWDERS OF POSSIBLE B-LFP MATERIALS.....</b>	<b>18</b>
<b>2.3.1 CS<sub>2</sub>SNI<sub>6</sub> MICROCRYSTALLINE POWDER.....</b>	<b>18</b>
<b>2.3.2 SN-DOPED CSBR MICROCRYSTALLINE POWDER .....</b>	<b>19</b>
<b>2.3.3 SB<sup>3+</sup>-DOPED DOUBLE PEROVSKITE POLYCRYSTALLINE POWDERS OF CS<sub>2</sub>NAINCL<sub>6</sub>, CS<sub>2</sub>KINCL<sub>6</sub>, CS<sub>2</sub>INBR<sub>5</sub>.....</b>	<b>21</b>
<b>3. CONCLUSIONS.....</b>	<b>22</b>





## 1 DELIVERABLE DESCRIPTION

---

Deliverable number	Deliverable title	WP number	Lead beneficiary	Due Date (in months)	Means of verification
D1.3	Homogeneous thin films of B-LFP nanocrystals and properties	WP1	1 - UVEG	12	Laboratory data regarding the successful preparation of homogeneous thin films of BLFP nanocrystals and investigation of their optical properties





## 2 RESULTS ON DIFFERENT PEROVSKITE MATERIALS

This section briefly describes the laboratory data regarding different successful preparation of homogeneous thin films of B-LFP nanocrystals and investigation of their optical properties, which prove the D1.3 fulfilment. Table 1 lists the optical properties of: (1) thin layers of five types of nanocrystals, considered by us as possible **benchmark lead free perovskite (B-LFP)** materials (materials 1-5), as well as (ii) five types of microcrystalline powders that are potential candidates on **B-LFP** materials (materials 6-10, in Table 1 they are marked with a beige background). The fabrication of thin layers of nanocrystals 1-5 is described in Section 2.1, and the optical properties of each of them are detailed in the following sections. Layers of the following nanocrystals are recognized as promising materials for further research:  $\text{FASnI}_3$ ,  $\text{Ag}_2\text{BiI}_5$  and  $\text{Ag}_3\text{BiI}_6$ , in Table 1 they are marked with a green background.

**Table 1.** Materials and description of their main structural and optical features.

	Material	Synthesis method, morphology	Absorption Exciton resonance	PL peak Wavelength (nm)	PLQY (*) in film at room temperature	Partners
1	$\text{FASnI}_3$ (FA is forma- midinium)	Hot-injection, nanoparticles 7-12 nm	700	725	<5%	ETHZ, SRI
2	$\text{Cs}_2\text{SnI}_6$	Ball milling, nanoparticles 8-14 nm	623 nm 1.99 eV	735	Extremely low	AVA, UVEG, UB
3	$\text{Ag}_2\text{BiI}_5$	Ball milling, nanoparticles	560 nm 2.20 eV	730	~2.5%	AVA
4	$\text{Ag}_3\text{BiI}_6$	Ball milling, nanoparticles	560 nm 2.20 eV	730	~2.5%	AVA
5	$\text{Cs}_3\text{Bi}_2\text{I}_9$	Laser ablation in liquid, nanoparticles 8-10 nm	479 nm 2.60 eV	510	Extremely low	UVEG
6	$\text{Cs}_2\text{SnI}_6$	Direct precipitation reaction, microcrystalline powder	663 nm 1.87 eV	900-1100	Low	UJI, UB, UVEG
7	Sn-doped $\text{CsBr}$	Direct precipitation reaction, microcrystalline powder	424 nm 2.92 eV	612	20%	UJI, UB, UVEG
8	$\text{Cs}_2\text{NaInCl}_6$	Chemical synthesis, microcrystalline powder	318 nm 3.90 eV	446	75%	ETHZ
9	$\text{Cs}_2\text{KInCl}_6$	Chemical synthesis, microcrystalline powder	321 nm 3.86 eV	493	50%	ETHZ
10	$\text{Cs}_2\text{InBr}_5$	Chemical synthesis, microcrystalline powder	358 nm 3.46 eV	673	25%	ETHZ

(\*) PLQY – PhotoLuminescence Quantum Yield



## 2.1 Preparation of films

Nanocrystals of five different types of the lead-free perovskites, promising for the purposes of this Project (see Table 1, lines 1-5), were manufactured by partners in the form of colloidal dispersions. The optical properties of these dispersions were preliminarily investigated in the laboratories of the partners immediately after the synthesis of nanocrystals. Within the framework of this Deliverable, we investigated the optical properties of thin solid-state films obtained from the above-mentioned colloidal nanocrystals by deposition on the surface of a glass substrate.

For optical study of films, as well as for their further use in various devices, their optical homogeneity is required, which is determined by the used method of film deposition, as well as by the adhesion of nanocrystals relative to the substrate surface. Within the framework of this Deliverable, we used such low demanding deposition methods for producing thin films as drop casting, spin coating, and dip coating. The first two methods were used to obtain films of  $\text{Cs}_2\text{SnI}_6$ ,  $\text{Ag}_2\text{BiI}_5$ , and  $\text{Ag}_3\text{BiI}_6$  nanocrystals, while for the deposition of  $\text{FASnI}_3$  nanocrystals the most suitable method is spin coating, and for  $\text{Cs}_3\text{BiI}_9$  nanocrystals, the dip coating method.

Figure 1 shows photographs of  $\text{Ag}_2\text{BiI}_5$  (a),  $\text{Ag}_3\text{BiI}_6$  (b), and  $\text{Cs}_2\text{SnI}_6$  (c) nanocrystal films deposited onto  $2.5 \times 2.5 \text{ cm}^2$  glass substrates by the drop casting method followed by delayed evaporation of the solvent (toluene). To slow down the evaporation of toluene, the substrates were placed on the bottom of a glass Petri dish, which was covered from above with a larger Petri dish. The numbers 1, 2 and 3 on the substrates indicate the number of drops of the concentrated colloidal dispersion (concentration 50-60 mg/mL for  $\text{Ag}_2\text{BiI}_5$  and  $\text{Ag}_3\text{BiI}_6$  and 25 mg/mL for  $\text{Cs}_2\text{SnI}_6$ ).

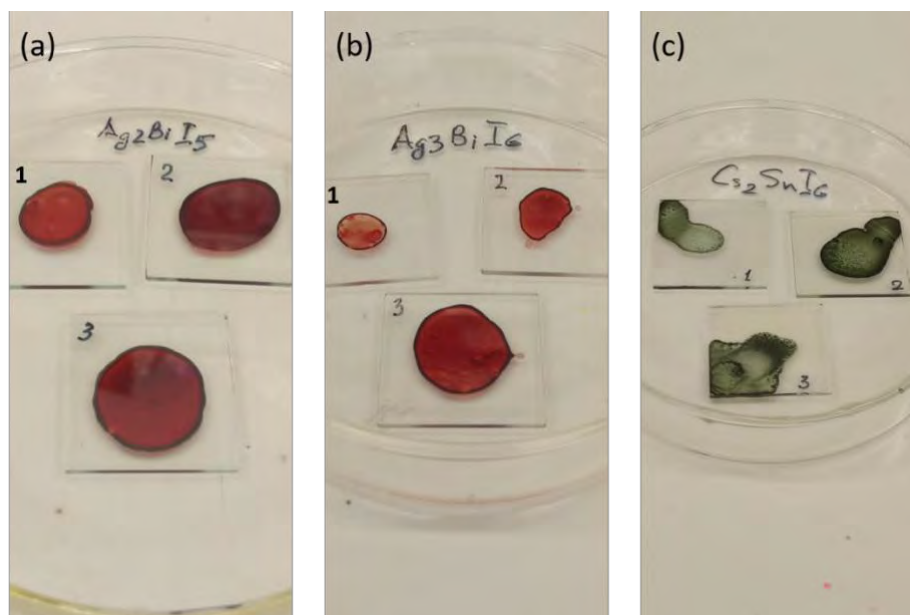


**Figure 1.** Photographs of the films of  $\text{Ag}_2\text{BiI}_5$  (a),  $\text{Ag}_3\text{BiI}_6$  (b), and  $\text{Cs}_2\text{SnI}_6$  (c) deposited on the surface of  $2.5 \times 2.5 \text{ cm}^2$  glass substrates by the drop casting method followed by delayed evaporation of the solvent (toluene). The numbers 1, 2 and 3 on the substrates indicate the number of drops of the concentrated colloidal dispersions applied to form the layers.





In the case of  $\text{Ag}_2\text{BiI}_5$  (a) and  $\text{Ag}_3\text{BiI}_6$  (b) nanocrystals, the films obtained are of satisfactory optical quality, which is quite sufficient for performing luminescence measurements. Using a profilometer, we estimated the average film thicknesses as  $\approx 120$  nm (1 drop) and  $\approx 210$  nm (2 and 3 drops) for  $\text{Ag}_2\text{BiI}_5$  and  $\approx 80$  nm (1 drop),  $\approx 120$  nm (2 drops) and  $\approx 150$  nm (3 drops) for  $\text{Ag}_3\text{BiI}_6$ . In the case of  $\text{Cs}_2\text{SnI}_6$  nanocrystals (Fig. 1c), the films turned out to be very inhomogeneous, which is most likely due to differences in the adhesion capacity of these nanocrystals.

Figure 2 shows photographs of films of  $\text{Ag}_2\text{BiI}_5$  (a),  $\text{Ag}_3\text{BiI}_6$  (b), and  $\text{Cs}_2\text{SnI}_6$  (c) nanocrystals deposited on  $2.5 \times 2.5$  cm<sup>2</sup> glass substrates by spin coating. For this, 100  $\mu\text{L}$  of a concentrated dispersion is deposited on the substrate with its subsequent rotation at a rate of 3000 rpm (a row of samples closest to the bottles) or 1000 rpm (a row closest to the viewer) during 1 min. The resulting films were of high optical uniformity, and their thicknesses were estimated using a profilometer as  $\approx 35$  and  $\approx 50$  nm for  $\text{Ag}_2\text{BiI}_5$ ,  $\approx 30$  and  $\approx 45$  nm for  $\text{Ag}_3\text{BiI}_6$ , and  $\approx 20$  and  $\approx 30$  nm for  $\text{Cs}_2\text{SnI}_6$  at substrate rotation rates of 3000 and 1000 rpm, respectively.

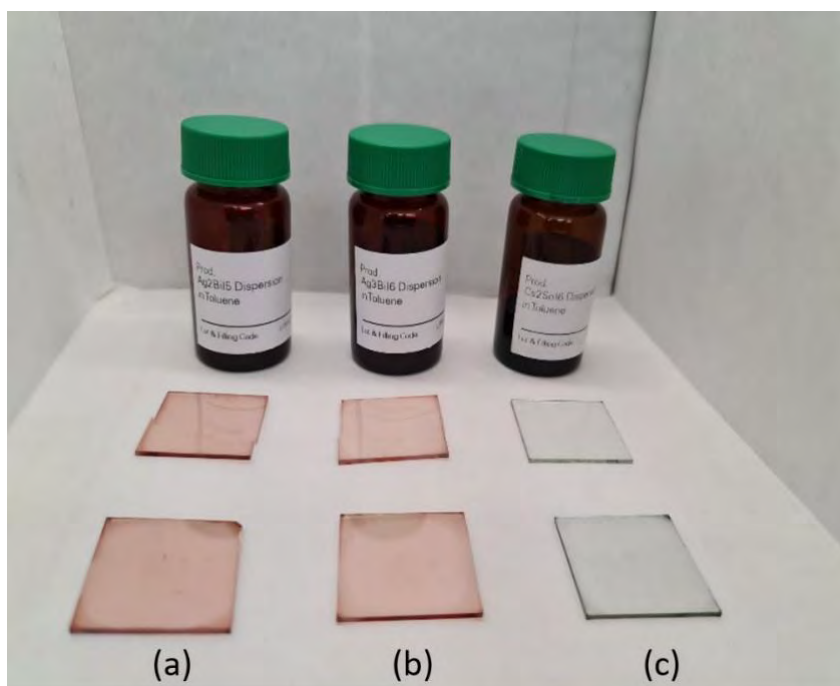


**Figure 2.** Photographs of films of  $\text{Ag}_2\text{BiI}_5$  (a),  $\text{Ag}_3\text{BiI}_6$  (b), and  $\text{Cs}_2\text{SnI}_6$  (c) nanocrystals deposited on  $2.5 \times 2.5$  cm<sup>2</sup> glass substrates by spin coating. For this, a 100  $\mu\text{L}$  of concentrated dispersion is deposited onto the substrate followed by its rotation at a speed of 3000 rpm (a row of samples closest to the bottles) or 1000 rpm (a row of samples closest to the viewer) during 1 min. Also shown are containers made of tinted glass, in which these suspensions were supplied to us by Avantama.

As for the production of films of  $\text{FASnI}_3$  nanocrystals, since these nanocrystals are subject to rapid irreversible oxidation and destruction in the presence of trace amounts of oxygen and water, the production of the films was carried out in a glovebox in a highly purified nitrogen atmosphere. In





order to make the results more reproducible, we used only the spin coating method for the deposition of  $\text{FASnI}_3$  nanocrystals. A detailed description of thin films made of this material, as well as the corresponding photographs, are given in the next section. Here we can state that the layers of  $\text{FASnI}_3$  nanocrystals demonstrate good optical uniformity at thicknesses of the order of 40-100 nm.

To study the optical properties (in particular, photoluminescence) of films of  $\text{Cs}_3\text{Bi}_2\text{I}_9$  nanocrystals, we used the dip coating method. The point is that we did not register any photoluminescence for these nanocrystals during the production of films by the drop casting and spin coating methods, and only when the effective layer thickness was reduced to values smaller than the nanocrystal diameter, the narrow-band PL was detected at low temperatures. For this reason, we put forward the assumption that the absence of PL in thicker layers is due to aggregation of nanocrystals, and therefore the subsequent samples were prepared by the dip coating method. Using this method, it is possible to achieve very low concentrations of nanocrystals adsorbed on the glass surface, so that we can talk about single nanocrystals or their small aggregates on the substrate surface. The results of luminescence measurements obtained in this case are described in one of the following sections.

Finally, in addition to the production and study of the optical properties of thin films of five different types of nanocrystals, which we considered a priori candidates as B-LFP and/or first generation of LFP materials (materials 1-5 in Table 1), we also studied the luminescence properties of five other possible LFP materials synthesized in the form of microcrystalline beads (materials 5-10 in Table 1). We investigated these powders within the framework of the Deliverable, because these materials, in principle, could turn out to be alternative candidates for (most probably) next future G-LFP materials, but due to lack of time, we were not able to produce such a large amount of additional materials in the form of colloidal nanocrystals (this process is time-consuming, since it requires careful selection of both synthesis conditions and passivating ligands on the surface of nanoparticles) and necessary to discuss within the Consortium which ones will be selected for further work. As a result, we settled on the study of the photoluminescent properties of these materials in the form of microcrystals, since the analysis of these results allowed us to conclude that their further study as possible candidates for (most probably) G-LFP materials is advisable or not feasible. In this case, microcrystals of these five materials were deposited on the substrate surface by drop casting from a suspension of microcrystals in toluene followed by evaporation of toluene.

## 2.2 Optical properties of thin films of possible B-LFP nanocrystals

### 2.2.1 Films of Tin (Sn)-based perovskite nanocrystals: $\text{FASnI}_3$

*Synthesis.*  $\text{FASnI}_3$  is the most promising compound among the other tin (II) halide perovskites. Colloidal synthesis of monodisperse  $\text{FASnI}_3$  NCs with size in range 7-12 nm has been developed. Various solvents including octadecene (ODE), toluene, mesitylene and Dowtherm A were used for the synthesis. Synthesis in Dowtherm A works with higher reproducibility as compared to ODE. Reasonably monodisperse NCs (Figure 3) were obtained after optimization of synthetic parameters (FA:Sn stoichiometry, concentration of oleic acid, temperature). As the inset in the Figure 3 shows,



PL spectra of the synthesized NCs depend on a solvent used that can be certainly transferred to the optical properties of the corresponding FASnI<sub>3</sub> NC films.

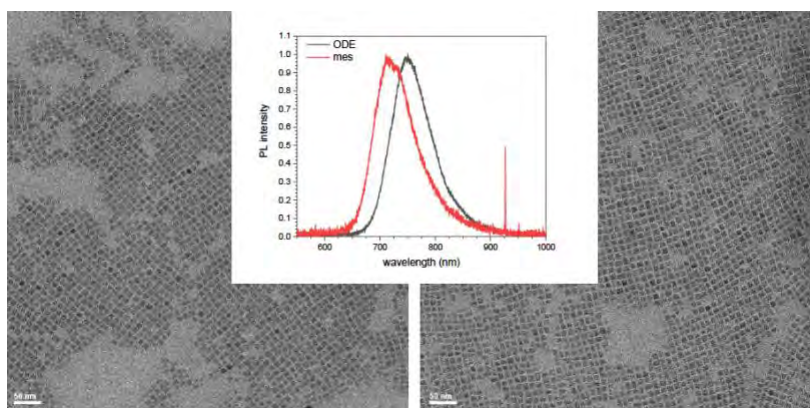


**Figure 3.** TEM images and PL spectra of FASnI<sub>3</sub> NCs synthesized in ODE (left) and mesitylene (right) with otherwise identical conditions. PL spectra of the both types of NCs are shown in the inset and demonstrate a dependence of the NC optical properties on a solvent used for synthesis.

The injection temperature allows the tuning of the nanocrystal size in the range 7 – 10 nm from 100 to 40 °C. However, PL does not change significantly (Figure 4), either because this size range is still within the weak confinement regime or because emission is defect-assisted. The possible presence of Sn<sup>4+</sup> defects, which may essentially deteriorate optical and electronic properties of the material, has been investigated by means of addition of various antioxidants and reducing agents. Particularly, FASnI<sub>3</sub> NCs have been treated with weak and strong reducing agents with concentrations varied in 3 orders of magnitude. Furthermore, synthesis in presence of antioxidants and reducing agents has been successfully performed. In all these cases, optical properties of NCs remain the same, indicating that potential Sn<sup>4+</sup> traps may be not the major traps in these NCs.

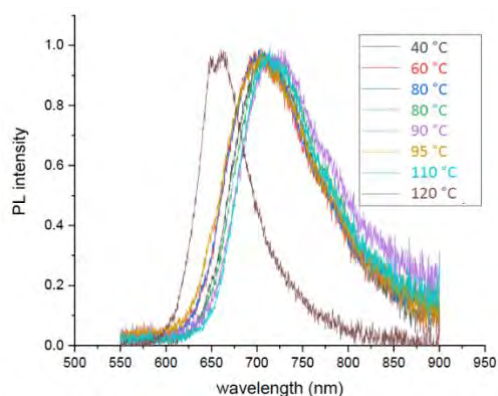


**Figure 4.** PL spectra of FASnI<sub>3</sub> NCs synthesized at different temperatures. All NCs synthesized in temperature range 40-110 C are colloiddally stable and have a size in the range of 7-10 nm.



**Film preparation.** Nanoparticles (NPs) of  $\text{FASnI}_3$  have been synthesized and characterized by DROP-IT partners ETH Zürich. These nanoparticles have been sent to SRI to be deposited by low demanding deposition methods (spin-coating/inkjet printing) and characterized by means of scanning electron microscopy (SEM), X-ray diffraction (XRD) and steady-state photoluminescence (SS-PL) in the thin film state to extract information on morphology, crystallinity and optoelectronic properties of the thin film samples.

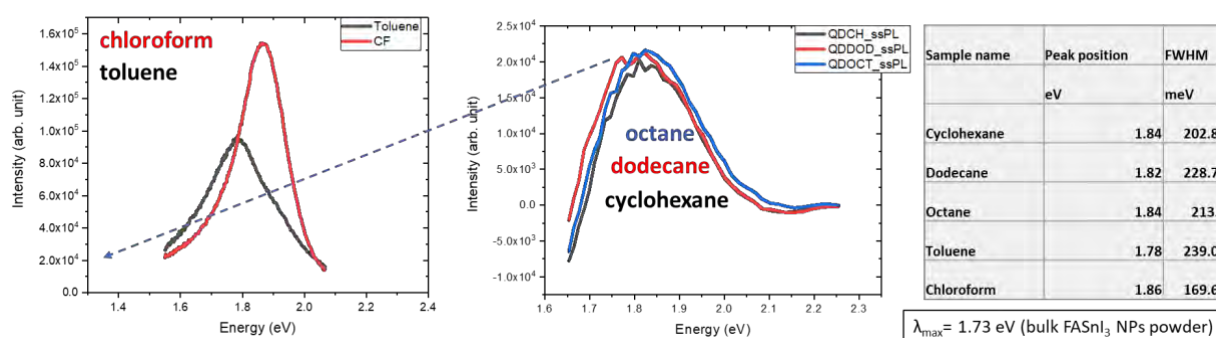


**Figure 5.** Steady state-photoluminescence spectra of  $\text{FASnI}_3$  NPs thin films (left) obtained from chloroform and toluene dispersions, (middle) obtained from octane, dodecane, cyclohexane dispersions. (right) Table summarizing the SS-PL emission peak position and the respective FWHM values.

In order to study the compatibility with the substrate,  $\text{FASnI}_3$  NPs have been dispersed in anhydrous toluene at an optimized concentration of 60 mg/mL and subsequently spin coated (at a speed of 2000 rpm for a duration of 30 seconds) on glass/ITO/PEDOT:PSS substrates and on glass substrates (for comparison) in a nitrogen filled glovebox with water and oxygen levels below 1ppm. The annealing influence has been assessed by direct thermal annealing of the obtained layers at 90 °C for 30 minutes in nitrogen atmosphere. The solvent influence on the  $\text{FASnI}_3$  layers has been studied by dispersing the  $\text{FASnI}_3$  NPs in six low polarity anhydrous solvents such as anisole, chloroform, toluene, dodecane, cyclohexane and octane at a concentration of 60 mg/mL. From the different experiments performed, the main results with focus on the basic electro-optical properties to foresee the potential for optoelectronic devices are the following:

The  $\text{FASnI}_3$  NPs were dispersible in the chosen low polarity solvents, except for the case of anisole (suspension). The energy bandgap of the obtained films measured by SS-PL was in the range of 1.76-1.86 eV (Figure 5), deviating substantially from the ideal bandgap of 1.4 eV (Shockley-Queisser) targeted for photovoltaic applications.

The lowest FWHM value of 169.64 meV along with the highest photoluminescence intensity was observed for  $\text{FASnI}_3$  NPs thin films deposited from chloroform dispersions. The FWHM values for the residual solvents were between 213.60 meV (octane) -239.06 meV (toluene). The SS-PL intensity of the  $\text{FASnI}_3$  NPs thin films decreased in the following order chloroform > toluene >> octane, dodecane, cyclohexane.



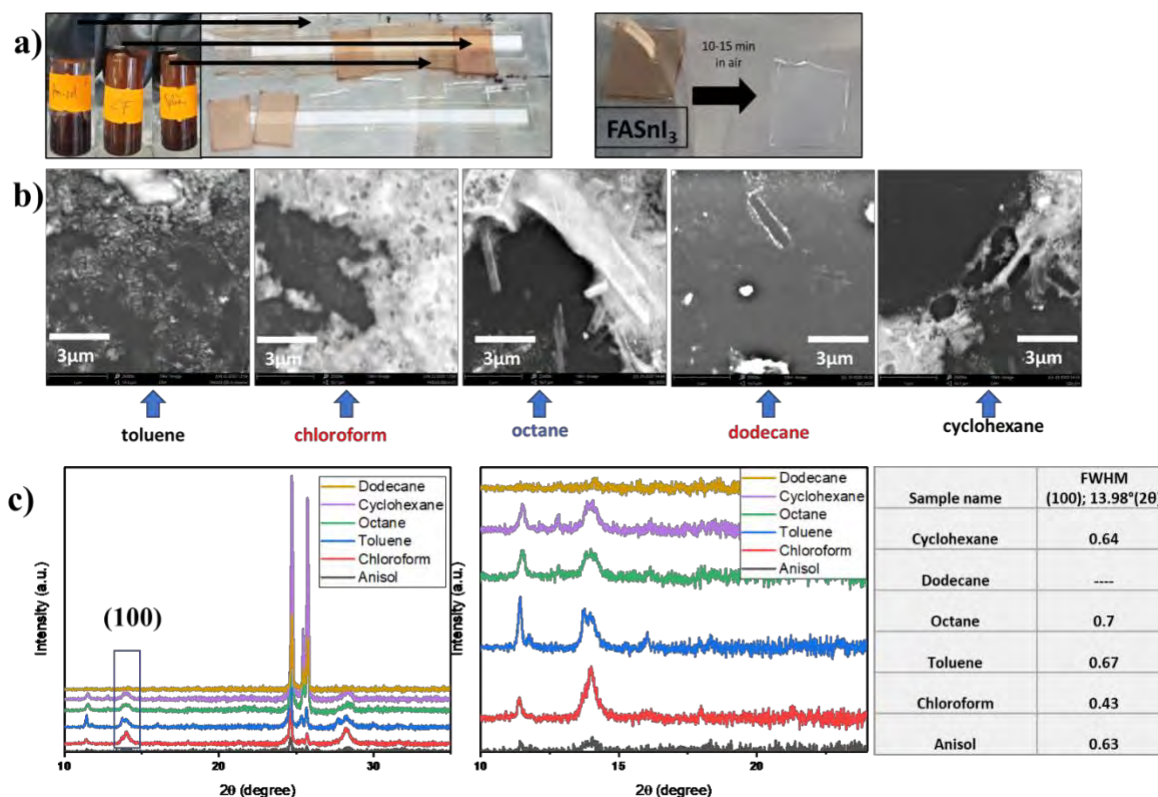


**Figure 6.** a) FASnI<sub>3</sub> NPs in (f.l.t.r.) anisole, chloroform and toluene solvent and pictures of the resulting FASnI<sub>3</sub> NPs thin films deposited on glass substrates. (right) Degradation of FASnI<sub>3</sub> NPs thin film exposed to ambient environment. b) SEM images of FASnI<sub>3</sub> NPs thin films obtained from toluene, chloroform, octane, dodecane and cyclohexane dispersions. c) XRD patterns of FASnI<sub>3</sub> NPs thin films obtained from toluene, chloroform, octane, dodecane, cyclohexane dispersions and anisol (suspension). (right) Table summarizing the FWHM values of the FASnI<sub>3</sub> perovskite Bragg reflection (100) observed at 13.98° (2θ).

The layers of FASnI<sub>3</sub> NPs were extremely sensitive to degradation upon air exposure (rapid oxidation of Sn<sup>2+</sup> to Sn<sup>4+</sup>), making it challenging to draw precise conclusions on which processing conditions are the best suitable to achieve the desired optoelectronic and morphological properties in view of future photovoltaic device integration efforts. After only 10-15 minutes the FASnI<sub>3</sub> NPs films turned from their characteristic dark red/brown colour to transparent (Figure 6a).

Although the FASnI<sub>3</sub> NPs layers were optically sufficiently homogeneous on the macroscale (Figure 6a, left), the layer morphology was found to be non-uniform on the micro-scale as evident from the SEM images of the FASnI<sub>3</sub> NPs thin films deposited from toluene, chloroform, octane, dodecane and cyclohexane dispersions, making it challenging to obtain high-quality layers for realizing long lasting and highly efficient photovoltaic devices (Figure 6b).

The influence of post deposition thermal treatment in nitrogen atmosphere was tested for FASnI<sub>3</sub> NPs thin films deposited from toluene dispersions. The XRD patterns of the thermally annealed sample (90 °C, 20 minutes) and the non-annealed standard samples are displayed in Figure 7. The





thermal annealing step reduced the XRD peak intensity for all observable Bragg peaks compared to the non-annealed sample, indicating a thermally induced degradation of the FASnI<sub>3</sub> NPs thin films. In particular, the peak intensity of the (111) and (200) reflections, observed at 25.26 ° and 26.37 ° (2θ) respectively were decreased to the greatest extent. The SS-PL intensity, peak position (annealed 1.77 eV; non-annealed 1.79 eV) were found to be similar among the samples, whereas the FWHM of the PL peak was slightly lower for the non-annealed sample (306.5 meV) vs. annealed (351.5 meV).

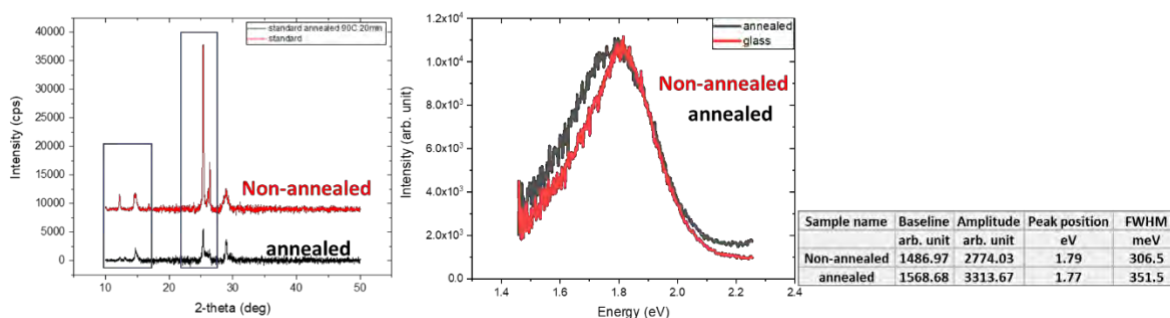


**Figure 7.** (left) XRD patterns of annealed (90 °C, 20 min.) and non-annealed FASnI<sub>3</sub> NPs thin films (deposited using toluene-based dispersion). (middle) SS-PL spectra of annealed (90 °C, 20 min.) and non-annealed FASnI<sub>3</sub> NPs thin films (deposited using toluene-based dispersion). (right) table summarizing the detected emission peak maximum.

The influence of the underlying substrate on the FASnI<sub>3</sub> NPs thin films (deposited using toluene dispersion) was assessed by comparing bare glass vs. glass/ITO/PEDOT:PSS substrates. The FWHM of the (100) diffraction peak was found lower in value for the glass substrate (0.5) compared to glass/ITO/PEDOT:PSS substrate (0.72). An influence on the XRD-peak intensity in dependence of the substrate was not observed, pointing towards a good compatibility of the FASnI<sub>3</sub> NPs with hole transport material PEDOT:PSS.

In summary, among the investigated solvents, the most promising results on FASnI<sub>3</sub> NPs thin films in terms of crystallinity and photoluminescence intensity were achieved with chloroform-based dispersions.

From the results presented in Table 2 an increase of the FWHM of the (001) perovskite peak (“XRD FWHM”) is observed when the FASnI<sub>3</sub> NP are deposited on the PEDOT/ITO/glass compared to glass substrate (samples 1 and 2). This result tends to indicate a higher crystalline quality of the samples deposited on glass. However, a decrease of the PL spectra FWHM (“PL FWHM”) is observed when the FASnI<sub>3</sub> NP are deposited on the PEDOT/ITO/glass substrate, this is in contradiction with the results observed by XRD.

Concerning the effect of the annealing, the results presented in Table 2 show a decrease of the XRD FWHM when the FASnI<sub>3</sub> films are annealed (samples 3 and 4). This result tends to indicate a higher crystalline quality of the annealed samples. In contradiction, an increase of the PL FWHM is observed when the FASnI<sub>3</sub> films are annealed. This contradiction might be related to the film’s





sensitivity to air exposure and the fast degradation of samples while measuring as evidenced in Figure 5.

**Table 2.** Summary of the main processing conditions and layer parameters extracted from the performed characterization. XRD FWHM refers to the full width at half maximum (FWHM) of the (001) perovskite peak, PL is characterized by the PL band position (PL peak) and FWHM of the PL spectrum.

Sample number	Solvent	Substrate	Annealing	XRD FWHM	PL peak	PL FWHM
				degree	eV	meV
1	Toluene	glass	No	0.5	1.79	306.5
2	Toluene	PEDOT / ITO / Glass	No	0.72	1.76	164.2
3	Toluene	glass	No	0.53	1.79	0.53
4	Toluene	glass	Yes	0.44	1.77	0.44
5	Cyclohexane	glass	No	0.64	1.84	202.9
6	Dodecane	glass	No	...	1.82	228.8
7	Octane	glass	No	0.7	1.84	213.6
8	Toluene	glass	No	0.67	1.78	239.1
9	Chloroform	glass	No	0.43	1.86	169.6
10	Anisole	glass	No	0.63	...	...

## 2.2.2 Films of Tin (Sn)-based perovskite nanocrystals: $\text{Cs}_2\text{SnI}_6$

By means of such a simple mechanochemical synthesis method as ball milling, we produced surface-passivated  $\text{Cs}_2\text{SnI}_6$  nanocrystals (Avantama). Tin atom in this compound should be in its oxidized  $\text{Sn}^{4+}$  form that suggests high environmental stability of these NCs. As our TEM investigations show (UVEG), the produced  $\text{Cs}_2\text{SnI}_6$  NC samples are inhomogeneous and mainly composed of hexagonal-like nanoparticles with 8 to 14 nm size (Figure 8, left) with some admixture of much bigger hexagonal NCs with 50 – 70 nm size (Figure 8, right). Analysis of our HRTEM data showed that the small and big NCs are of different chemical structures: whereas small NCs are identified as  $\text{Cs}_2\text{SnI}_6$  structures (Figure 9, left), big NCs have  $\text{CsSnI}_3$  structure (Figure 9, right).



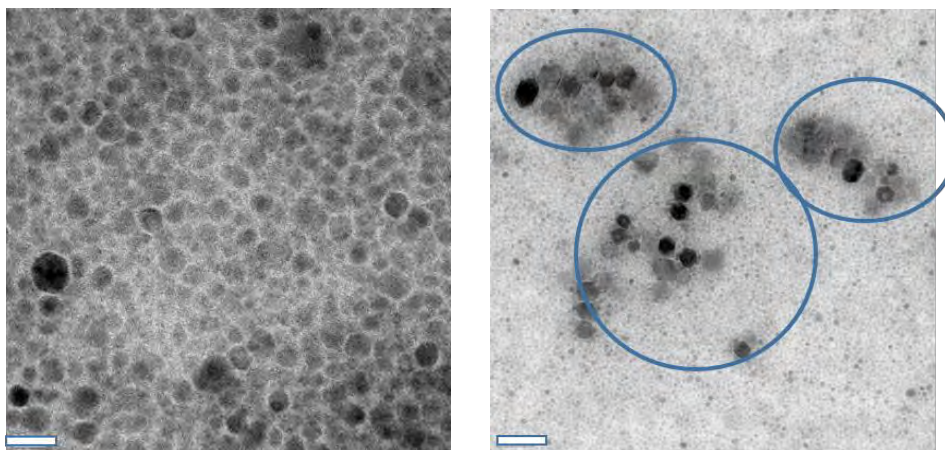


**Figure 8.** TEM images of a sample of  $\text{Cs}_2\text{SnI}_6$  NCs produced by ball milling: small NCs of 8-14 nm diameter were found (right image, scale bar 20 nm) with an admixture of big NCs with 50-70 nm diameter (left image, scale bar 100 nm).

### $\text{Cs}_2\text{SnI}_6$ ( $\text{Sn}^{4+}$ ) NCs are inhomogeneous – HRTEM data

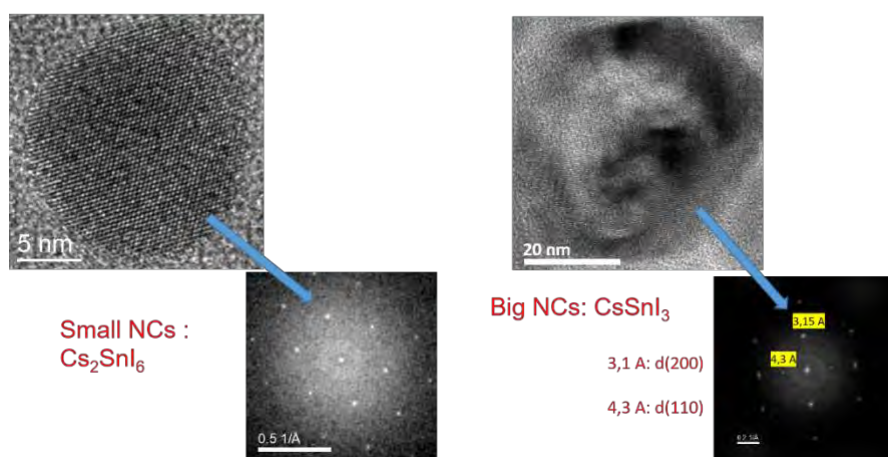


**Figure 9.** HRTEM images of a sample of  $\text{Cs}_2\text{SnI}_6$  NCs enabling to identify small NCs as  $\text{Cs}_2\text{SnI}_6$  structures (left images) and big NCs as  $\text{CsSnI}_3$  structures (right images).

Absorption and PL spectra of a  $\text{Cs}_2\text{SnI}_6$  NCs sample prepared as a thin film deposited on glass by drop-casting are presented in Figure 10 (left). The absorption spectrum with a long-wavelength band at 623 nm (1.99 eV) certainly belongs to the small-size  $\text{Cs}_2\text{SnI}_6$  NCs. A very weak PL was detected only at 20 K for a  $\text{Cs}_2\text{SnI}_6$  NCs sample (red curve with a maximum of about 735 nm (1.69 eV) in Figure 10, left). However, this PL was detected not on the entire surface of the sample, but only at some points. This fact suggests that the very weak emission does not belong to the main material of the sample (small-size  $\text{Cs}_2\text{SnI}_6$  NCs shown in Figure 8, left). It cannot belong, however, to the big-size  $\text{CsSnI}_3$  structures because bandgap of this material is at 1.30 eV. The PL decay kinetics

detected at 20K (Figure 10, right) consists of two phases with the time constants of  $\tau_1=0.75$  ns (relative amplitude  $A_1=0.65$ ) and  $\tau_2=29.4$  ns (relative amplitude  $A_2=0.35$ )

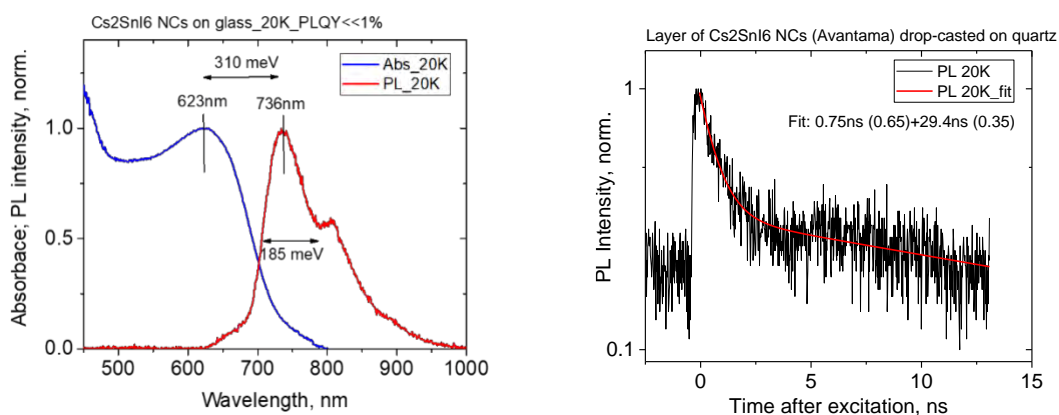


**Figure 10.** (left) Low temperature (20K) absorption and emission spectra and (right) PL decay kinetics of thin films of  $\text{Cs}_2\text{SnI}_6$  nanocrystals produced by ball milling.

Summarizing our observations on the  $\text{Cs}_2\text{SnI}_6$  NCs produced by ball milling, this material is not promising neither for photovoltaic, nor for lasing or optoelectronic applications because the synthesized 8-14 nm NCs do not demonstrate any detectable PL. It likely implies that the NCs contain high concentration of deep traps.

### 2.2.3 Films of $\text{Cs}_3\text{Bi}_2\text{I}_9$ nanocrystals

This  $\text{Cs}_3\text{Bi}_2\text{I}_9$  material has been initially prepared by mechanochemical synthesis (ball milling) as a powder by UVEG collaborators (group of Henk Bolink).<sup>[1]</sup> For transformation to nanocrystals, this powder was subsequently processed by fs-pulsed laser ablation in liquid (with appropriate ligands in solution) by the group of Andrei Kabashin from Aix-Marseille University (Marseille, France). Morphological, compositional and structural analysis of  $\text{Cs}_3\text{Bi}_2\text{I}_9$  NC samples were performed by high resolution transmission electron microscopy (HRTEM) with a field emission gun TECNAI G2 F20 microscope operated at 200 kV, having the capabilities of selected area electron diffraction (SAED) and energy dispersive X-ray spectroscopy (EDX) in the facilities of the Servei Central de Suport a la Investigació Experimental (SCSIE) at the University of Valencia. TEM images show that the samples are composed of uniform spherical-like nanocrystals of the average size of 8 – 10 nm (Figure 11). As HRTEM images and XRD and SAED analysis show (Figure 12), the  $\text{Cs}_3\text{Bi}_2\text{I}_9$  NCs are monocrystalline ones with a hexagonal structure.



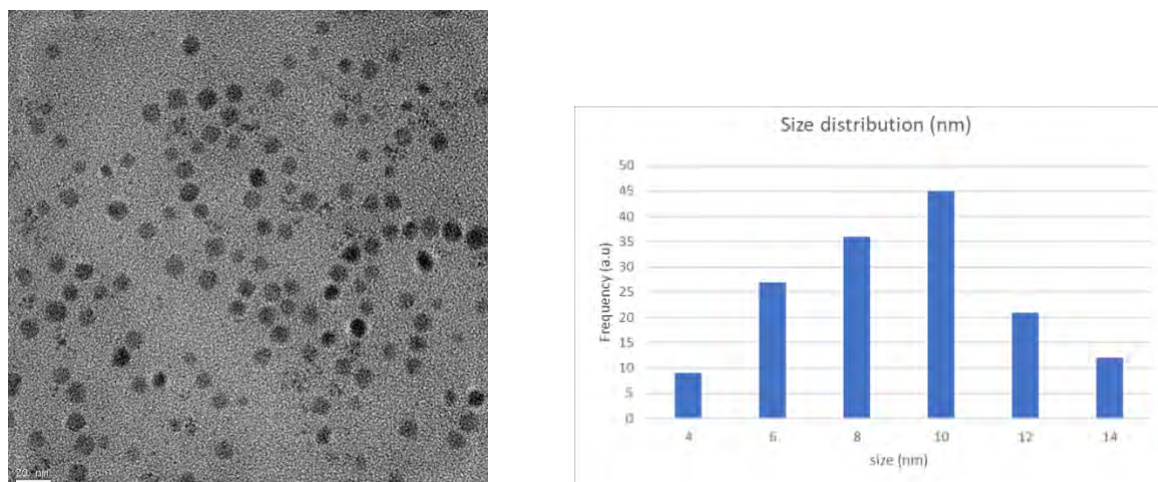


**Figure 11.** TEM image (left, scale bar 20 nm) and size distribution (right) of  $\text{Cs}_3\text{Bi}_2\text{I}_9$  NCs.

Thin films of  $\text{Cs}_3\text{Bi}_2\text{I}_9$  NCs were prepared by drop casting of the NC suspension in toluene on a quartz substrate. Absorption spectrum of such a film demonstrates a relatively narrow absorption band with a maximum at 478 nm (Figure 13, left). As far as the emission properties is concerned, the samples of  $\text{Cs}_3\text{Bi}_2\text{I}_9$  NCs showed narrow-band PL, but only in some points of a sample, not over all the surface. Besides, the PL emission is relatively strong only at cryogenic temperatures (integral PL intensity drops about 400 times when temperature grows from 20 to 300 K) and the PL spectra are generally different in different points of a sample with PL band maxima being in the region between 500 and 600 nm (Figure 13, left). With increasing temperature, the PL band width increases from 12 nm (53 meV) at 20 K up to 28.6 nm (137 meV) at 300 K (Figure 13, right).

### *HRTEM images of $\text{Cs}_3\text{Bi}_2\text{I}_9$ sample.*

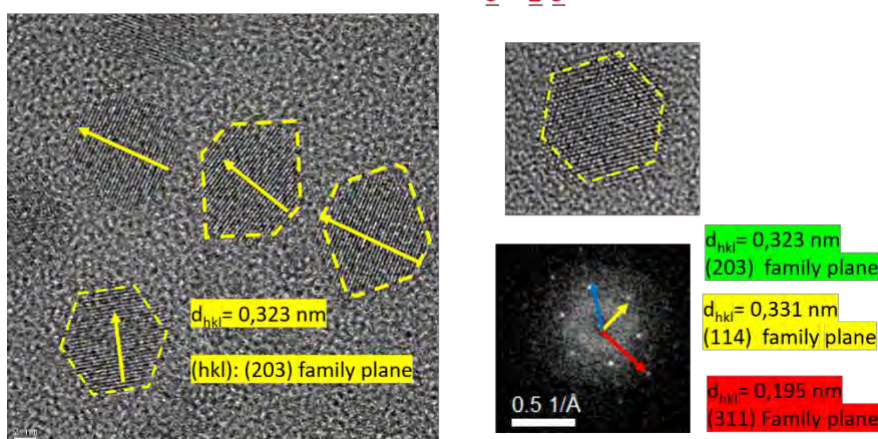


**Figure 12.** HRTEM images of  $\text{Cs}_3\text{Bi}_2\text{I}_9$  NCs.

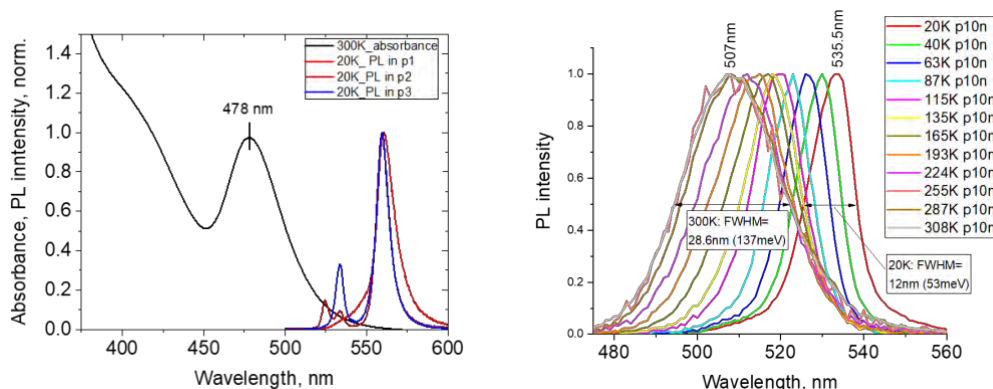


**Figure 13.** (Left) Absorption and PL spectra of a thin film of  $\text{Cs}_3\text{Bi}_2\text{I}_9$  NCs deposited on quartz substrate. (Right) Normalized PL spectra at different temperatures.

The work is in progress to determine an origin of such a luminescence, but our preliminary conclusion is that the  $\text{Cs}_3\text{Bi}_2\text{I}_9$  NCs produced by laser ablation are not promising for photovoltaic and optoelectronic applications because they have reasonably intensive PL only at cryogenic temperatures.

## 2.2.4 Films of nanocrystals of Rudorffites $\text{Ag}_2\text{BiI}_5$ and $\text{Ag}_3\text{BiI}_6$

Passivated nanocrystals of  $\text{Ag}_2\text{BiI}_5$  and  $\text{Ag}_3\text{BiI}_6$  Rudorffites were synthesized by ball milling (Avantama). The NC films were prepared by drop casting on quartz substrate. Note that the two materials demonstrated practically identical absorption and PL spectra (Figure 14). The long wavelength absorption band is detected at about 560 nm (2.2 eV), the room temperature emission is rather low-intensive (PLQY not higher than 2.5%) and its spectrum includes three bands (1.90, 1.70, and 1.40 eV), whereas at 20K the PL intensity grows about 40 times and spectrum exhibits two bands (1.70 and 1.40 eV). PL lifetime turned out to be very long (>100 ns). Our attempts to obtain an Amplified Spontaneous Emission (ASE) under powerful excitation at 532 nm were unsuccessful. Preliminary we suggest that the Rudorffite NCs can be suitable for photovoltaic applications, but optimization of their optical and electronic properties is required.

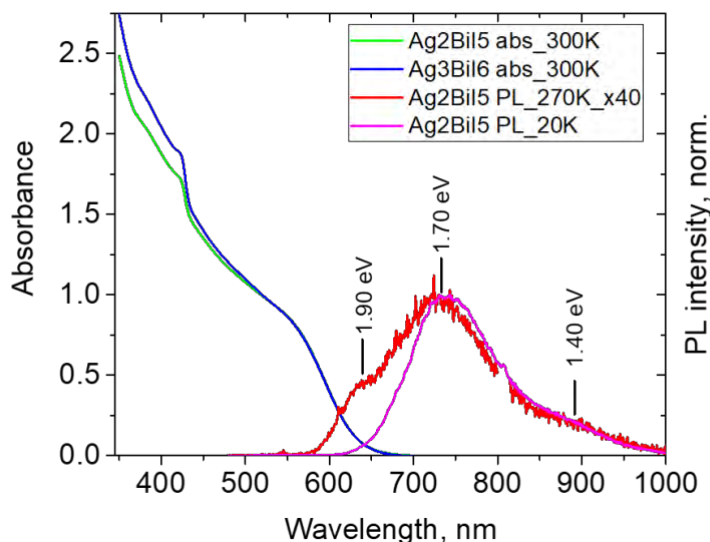


**Figure 14.** Absorption (blue and green lines) and PL spectra of  $\text{Ag}_2\text{BiI}_5$  and  $\text{Ag}_3\text{BiI}_6$  Rudorffites. Absorption is measured at room temperature, whereas PL is detected at both room and low temperatures.

## 2.3 Optical properties of microcrystalline powders of possible B-LFP materials

### 2.3.1 $\text{Cs}_2\text{SnI}_6$ microcrystalline powder

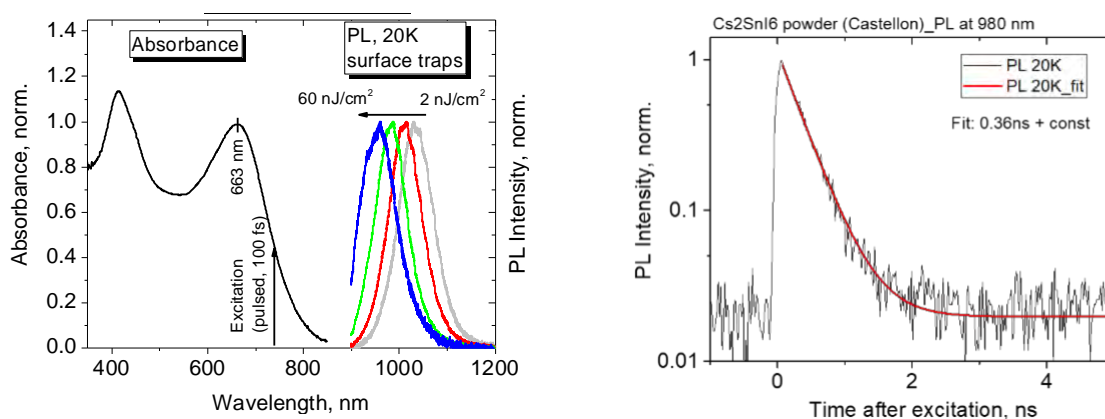


**Figure 15.** (Left) Absorption (black curve) and PL spectra at different fluencies (2 - 60  $\text{nJ}/\text{cm}^2$ , grey-red-green-blue continuous line curves) of  $\text{Cs}_2\text{SnI}_6$  powder. (Right) PL decay kinetics of  $\text{Cs}_2\text{SnI}_6$  powder measured at 980 nm (20K).





Microcrystalline powder of  $\text{Cs}_2\text{SnI}_6$  demonstrates the absorption edge at around 1.87 eV (663 nm, see the Figure 15, left), but emission is highly dependent on excitation power, which can be attributed to the trap defect states, which emit luminescence being red-shifted as compared to the real band edge state. At very high excitation power, when all defect (trap) states are populated, emission from the band edge state starts to prevail more and more. In this sense, the PL band observed at the highest excitation intensity (blue line) is close to the PL emission from the band edge state (960 nm or 1.29 eV) that well corresponds to the bandgap of 1.30 eV published earlier.<sup>[2]</sup> The PL decay kinetics with lifetime of 0.36 ns was also measured at 20K (Figure 6, right).

This microcrystalline powder material turned to be very stable in air conditions and can be further processed by ball milling and ultrasonication techniques for the preparation of thin films. The presented PL properties of the powder suggest that, after transformation either to microcrystalline film or to surface passivated NCs, this lead-free material may be promising for photovoltaic and/or optoelectronic applications (work in progress).

### 2.3.2 Sn-doped CsBr microcrystalline powder

By means of reaction of DMF-dissolved precursors CsBr and  $\text{SnBr}_2$  in aerated toluene in a flow reactor,  $\text{Cs}_2\text{SnBr}_6$  was formed which experienced oxidation to  $\text{Cs}_2\text{SnBr}_6$  and CsBr. At higher precursor ratio, phase pure CsBr XRD patterns were observed with inclusion of 3-5% of Sn that means that the synthesized material, which demonstrate bright yellow emission, is the material is Sn-doped CsBr.

We investigated the optical properties of Sn-doped microcrystalline CsBr powder in the temperature interval from 300 down to 20K. At room temperature the powder exhibits bright photoluminescence with the broad-band spectrum (FWHM of about 150 nm) centered at 612 nm (red line in Figure 16, left). The PL quantum yield (QY) of this emission is about 20% at room temperature when excited at 424 nm, that is in the center of the narrow PL excitation band (FWHM of about 35 nm, blue line in Figure 16, left). The PL Stokes shift between the PLE and PL spectra maxima is as large as 188 nm. All the above properties of the powder PL evidence in favor of a Sn-based impurity centers as an origin of the luminescence. The PL decay kinetics (Figure 16, right) was measured at 20K and turned out to be bi-exponential and rather long, with lifetimes  $\tau_1=2.6$  ns and  $\tau_2=26.7$  ns (relative amplitudes 0.87 and 0.13, respectively).

Although the PLQY measured under 424 nm excitation is rather high even at room temperature, under excitation at different wavelengths it seems to be much lower. Such a conclusion can be drawn from the analysis of the PL intensity dependence on temperature under excitation at 355 nm (Figure 11). Under these conditions the PL spectrum intensity demonstrates strong dependence on temperature, so that the integral PL intensity at 300K is only 3.7% of the intensity measured at 20K. If we suggest that at 20K the PLQY is  $\leq 100\%$ , it results in PLQY of  $\leq 3.7\%$  at 300K which is much lower than 20% measured under 424 nm excitation. Most likely, such low PLQY under excitation by photons with energy higher than the energy of the impurity center in absorption (424 nm) implies that, at these conditions, an essential part of the excitation is absorbed by the CsBr crystal matrix and nonradiatively degrades within the matrix at room temperature, but at low temperatures it is funneled to the impurity center to give the PL spectrum shown in Figure 11, left. Such a behavior is





not favorable for optical (lasing) and optoelectronic applications because at room temperature high PLQY can be achieved only under excitation within very narrow (about 30 nm) spectral interval around 424 nm.

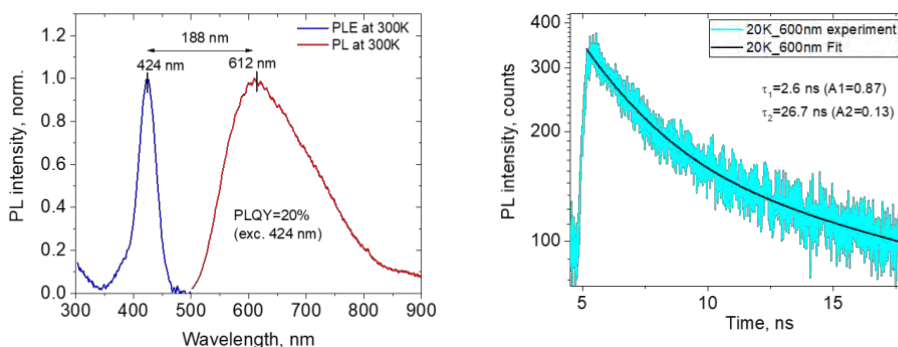


**Figure 16.** Optical properties of Sn-doped CsBr microcrystalline powder: PL and PLE spectra (left, both measured at 300K) and PL decay kinetics (right, measured at 20K).

Although the PLQY measured under 424 nm excitation is rather high even at room temperature, under excitation at different wavelengths it seems to be much lower. It may be concluded on the basis of analysis of the PL intensity dependence on temperature under excitation at 355 nm (Figure 17). Under these conditions the PL spectrum intensity demonstrates strong dependence on temperature, so that the integral PL intensity at 300K is only 3.7% of the intensity measured at 20K. If we suggest that at 20K the PLQY is  $\leq 100\%$ , it results in PLQY of  $\leq 3.7\%$  at 300K which is much lower than 20% measured under 424 nm excitation. Most likely, such low PLQY under excitation by photons with energy higher than the energy of the impurity center in absorption (424 nm) implies that, at these conditions, an essential part of the excitation is absorbed by the CsBr crystal matrix and nonradiatively degrades within the matrix at room temperature, but at low temperatures it is funneled to the impurity center to give the PL spectrum shown in Figure 17, left. Such a behavior is not favorable for optical (lasing) and optoelectronic applications because at room temperature high PLQY can be achieved only under excitation within very narrow (about 30 nm) spectral interval around 424 nm.



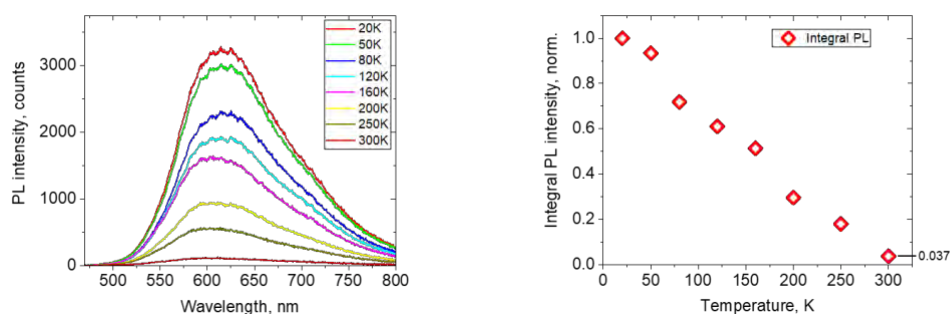


**Figure 17.** Optical properties of Sn-doped CsBr microcrystalline powder: temperature dependence of PL spectrum (left) and PL integral intensity (right). The PL excitation was realized by 1 ns pulses at 355 nm.

### 2.3.3 $\text{Sb}^{3+}$ -doped double perovskite polycrystalline powders of $\text{Cs}_2\text{NaInCl}_6$ , $\text{Cs}_2\text{KInCl}_6$ , $\text{Cs}_2\text{InBr}_5$

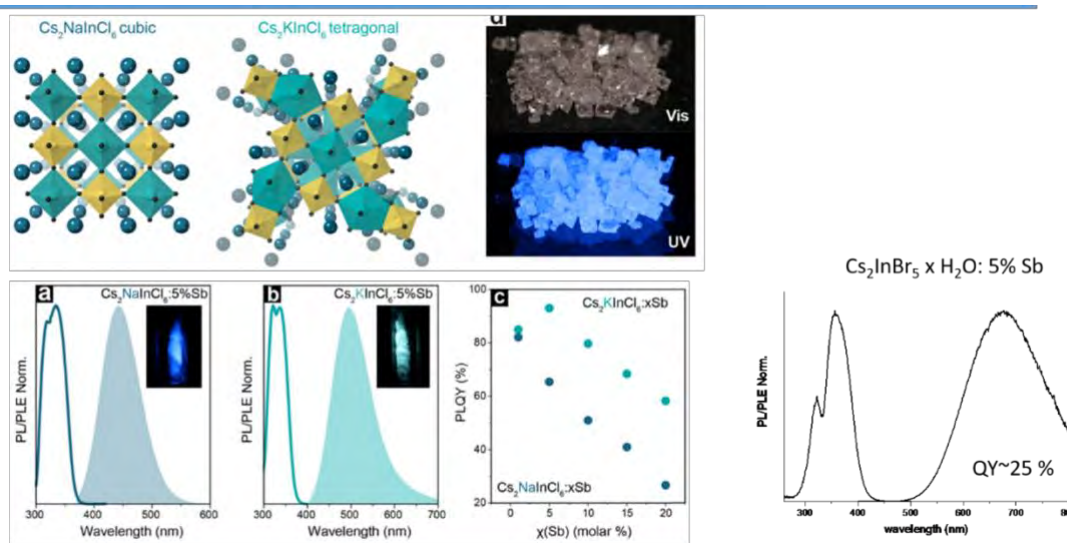


**Figure 18.** Crystal structure and room temperature PL and PLE spectra of  $\text{Cs}_2\text{NaInCl}_6$ ,  $\text{Cs}_2\text{KInCl}_6$ ,  $\text{Cs}_2\text{InBr}_5$  double perovskites doped with  $\text{Sb}^{3+}$ .

Microcrystalline powders of lead-free double perovskites  $\text{Cs}_2\text{NaInCl}_6$  (I),  $\text{Cs}_2\text{KInCl}_6$  (II),  $\text{Cs}_2\text{InBr}_5$  (III) doped with  $\text{Sb}^{3+}$  have been also synthesized with the aim to investigate their PL properties and find, if possible, conditions for achieving the Amplified Spontaneous Emission (ASE). In the above compounds the double perovskites structures serve as a host matrix for luminescent  $\text{Sb}^{3+}$  ions. The powders demonstrate rather broad PL spectra in the blue (I), blue-green (II), and red (III) regions



with the PLQY of about 75, 50, and 25%, respectively, when  $\text{Sb}^{3+}$  concentration is 5% (Figure 18). Low temperature PL spectra were measured for all three compounds under excitation by powerful 1 ns pulses at 355 nm and demonstrated additional red-shifted bands for the compounds I and II, but did not show any evidences of ASE (Figure 19). Note also that the PLQYs of all compounds measured at room temperature demonstrate strong dependence on the excitation wavelength (Figure 20) that makes difficult their practical applications in optoelectronics and lasing.

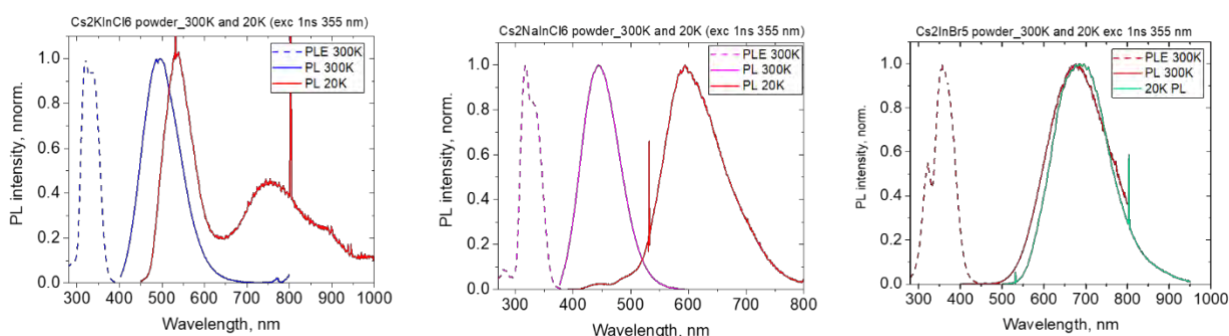


**Figure 19.** Room temperature PLE and room and low temperature PLE spectra of  $\text{Cs}_2\text{NalInCl}_6$ ,  $\text{Cs}_2\text{KInCl}_6$ ,  $\text{Cs}_2\text{InBr}_5$  double perovskites doped with  $\text{Sb}^{3+}$ .

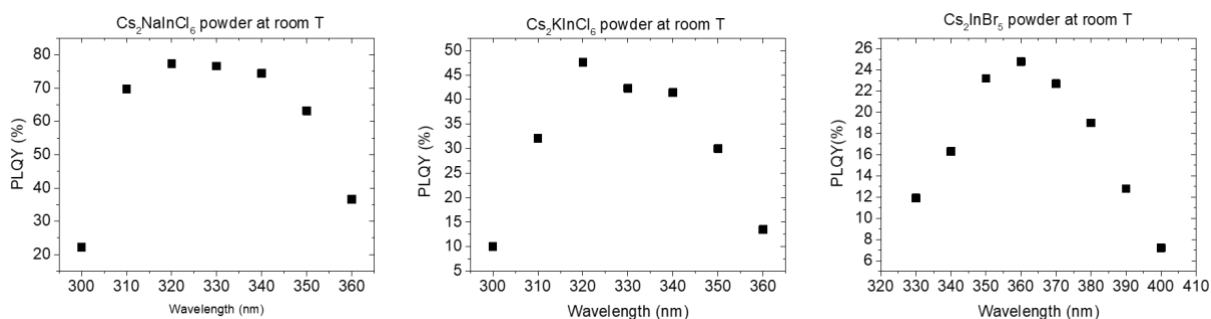


**Figure 20.** Room temperature dependence of PLQY on excitation wavelength for  $\text{Cs}_2\text{NalInCl}_6$ ,  $\text{Cs}_2\text{KInCl}_6$ ,  $\text{Cs}_2\text{InBr}_5$  double perovskites doped with  $\text{Sb}^{3+}$ .

### 3 CONCLUSIONS

Thus, more than ten LFP materials have been tested within DROP-IT activities of Tasks 1.1-1.2-1.3 in WP1 (see section 2) in order to investigate if they can be suitable for developing future devices, either photovoltaic (WP 3) or emitting ones (WPs 4-5). Research on some of these materials will be discontinued, and instead, research will begin on other, more promising materials.





After analysis of the results obtained with all studied nanocrystals and powders, nanoparticles of **FASnl<sub>3</sub>** and **Ag<sub>2</sub>BiI<sub>5</sub> - Ag<sub>3</sub>BiI<sub>6</sub>** (Rudorffites) are now being considered as the most promising candidates for future benchmark devices by using nanocrystals in solution. It is worth mention that the needs **FASnl<sub>3</sub>** processing (formation of films and fabrication of devices) in glove box. Meanwhile, further optimisation of the optical and morphological properties of Rudorffites is required.

## REFERENCES

- [1] Y. El Ajjouri, V. S. Chirvony, N. Vassilyeva, M. Sessolo, F. Palazon, H.J. Bolink. Low-dimensional non-toxic A<sub>3</sub>Bi<sub>2</sub>X<sub>9</sub> compounds synthesized by a dry mechanochemical route with tunable visible photoluminescence at room temperature, *J. Mater. Chem. C*, **2019**, 7, 6236-6240.
- [2] B. Lee, C. C. Stoumpos, N. Zhou, F. Hao, C. Malliakas, C.-Y. Yeh, T. J. Marks, M. G. Kanatzidis, R. P. H. Chang. Air-stable molecular semiconducting iodosalts for solar cell applications: Cs<sub>2</sub>SnI<sub>6</sub> as a hole conductor. *J. Am. Chem. Soc.* **2014**, 136, 15379-15385.

